Supplementary Information : Quantum sensing of opaque materials with plasmonically enhanced hBN spin defects

Saakshi Dikshit,[†] Sumukh Vaidya,[‡] Troy Tsubota,[‡,¶] Xingyu Gao,[‡] Peng Ju,[‡] Zhiyan Xie,[‡] Kunhong Shen,[‡] Naveed Hussain,[§] Shougo Higashi,[§,‖] Debasish Banerjee,[§] Songtao Wu,[*,§] and Tongcang Li[*,‡,†,⊥,#]

†*Elmore School of Electrical and Computer Engineering, Purdue University, West*
1 *Lafayette, Indiana 47907, USA*

‡*Department of Physics and Astronomy, Purdue University, West Lafayette, Indiana 47907, USA*

¶*Department of Physics, University of California, Berkeley, California 94720, USA*

§*Toyota Research Institute of North America, Ann Arbor, MI, USA 48105*

‖*Material Engineering Division, Toyota Motor Corporation, Aichi, Japan, 471-8572*

⊥*Birck Nanotechnology Center, Purdue University, West Lafayette, Indiana 47907, USA*

#*Purdue Quantum Science and Engineering Institute, Purdue University, West Lafayette, Indiana 47907, USA*

E-mail: songtao.wu@toyota.com; tcli@purdue.edu

Methods

Creation of V_B^- spin defects in hBN flakes

We purchase commercially available hBN crystal from 2D Semiconductors. The crystal is then exfoliated using blue tape. We transfer the exfoliated hBN flakes onto a 0.5 $cm \times 0.5$ cm clean silicon substrate by sticking the tape to the substrate and heating at 80°C for 10 minutes, till the tape loses stickiness. We then implant the hBN flakes transferred onto the silicon substrate with ionized helium gas using a home-built ion implantation system. The implantation system is based on the ion source ISIS3000 (PSP Vacuum Technology). We implant the flakes with a 2.5 keV beam of He^+ ions and calculate the approximate dosage to be $8.1 \times 10^{14}/cm^2$.

Fabrication of gold waveguide onto silica glass/sapphire coverslips

A gold microwave coplanar waveguide was fabricated on $130 - 170$ μm thick silica glass coverslips (Cole Parmer, EW-48511-00) using standard photolithography, followed by electron beam evaporation of a 30 nm (or 50 nm) gold layer. Prior to gold deposition, a 5 nm titanium adhesion layer was deposited onto the coverslip to improve the adhesion of the gold layer to the substrate. The width of the coplanar waveguide was 52.5 μm. Later, we switched to 100 μm thick sapphire coverslips (University Wafers, 4083) to reduce mechanical vibrations during microwave measurements. We also reduced the width of the coplanar waveguide to 25 μm to reduce the FIB fabrication time.

Fabrication of Nanoslit Array using Helium/Neon Focused Ion Beam

Fabrication of the nanoslit array was performed using the Zeiss Orion NanoFab Helium Ion Microscope (HIM)/Helium Focused Ion Beam(FIB). The helium FIB was used for imaging, whereas the neon FIB was used for patterning. The beam current typically used to pattern the nanoslit array was 1-3 pA. The typical dose of neon ions used was 2400-5000 ions/nm^2

and typical landing energy used was 25 keV.

Higher dosage (5000 ions/nm^2) combined with lower landing energy (15 keV) was used to pattern gold waveguides on sapphire coverslips, due to the crystalline nature of the substrate. To fabricated the 50 nm gold device, we used higher landing energy (25 keV) and higher neon ion dose (10000 ions/nm^2) to etch through the gold layer completely.

Confocal System and PL measurements

The optical measurements and photoluminescence measurements were done using a home-built confocal system. All measurements were performed under ambient conditions. A 532 nm laser was passed through a 532 nm line filter (Edmund Optics, 64-252) and then directed towards the sample using a 550 nm dichroic mirror (Thorlabs, DMLP550). A galvonometer optical scanner (Edmund Optics, ScannerMAX Compact 506) was used to scan the laser over the surface of the sample, which remained stationary on a mounting stage. The laser was focused onto the sample using a 0.9 NA 100X objective lens. An acousto-optic modulator (AOM) (Isomet, M1205-T110L-1) was used as a fast optical switch. The photoluminescence was filtered out from the laser path using the same 550 nm dichroic mirror. The signal was further filtered using 750 nm longpass filter (Thorlabs, FELH0750) and a 561 nm dichroic filter (Semrock, BLP02-561R-25). The signal was collimated into a multimode fiber (Thorlabs, M31L02) and sent to a single-photon detector (Excelitas, SPCM-AQRH) or a spectrometer (Andor Shamrock SR-500).

For measurements from the backside of the device, the objective lens was replaced by a 1.3 NA 100X oil objective lens (Olympus, RMS100X-PFO). A low-fluorescence oil was dropped between the coverslip and objective lens, through which the laser was focused onto the nanoslit array from the backside. The rest of the measurement set-up remained the same.

Optically Detected Magnetic Resonance Measurements

The microwave signals were generated by a signal generator (Stanford Research Systems SG386). Two fast RF switches (Mini-Circuits ZASWA-2-50DRA+) were used to modulate the microwave amplitude. The microwave signal was amplified using a MW amplifier (Mini-Circuits, ZHL-15W-422-S+) and then delivered to the device using gold-plated SMA connectors. All pulse sequences were generated by a pulse streamer (Swabian Instruments, Pulse Streamer 8/2).

COMSOL Simulations

Optical Simulations

We performed COMSOL simulations to optimize the optical performance of the nanoslit array. Supplementary Figures 1 (a) and 2 (a) show the side view of the simulation set-up for different hBN thicknesses (15 nm and 30 nm respectively) and implantation depths (10 nm and 25 nm respectively). All simulations are done for 830 nm wavelength, the emission wavelength for V_B^- defects.

The two figures-of-merit that we wanted to maximize was the transmission through the nanoslit array and the plasmonic enhancement inside the nanoslit. The plasmonic enhancement was calculated by taking a ratio of the normalized electric field intensity at the implantation depth ($E_{nanoslit}/E_{gold}$) as shown in Supplementary Figures 1 (a) and 2 (a). To determine the best nanoslit width and period, we performed parametric sweep of nanoslit width as a percentage of period from 0.2 to 0.85, and the period from 50 to 350 nm. We then plotted the plasmonic enhancement, the transmission and the product of the plasmonic enhancement and transmission as a contour plot to determine the design that would give us the maximum photoluminescence from the backside of the device.

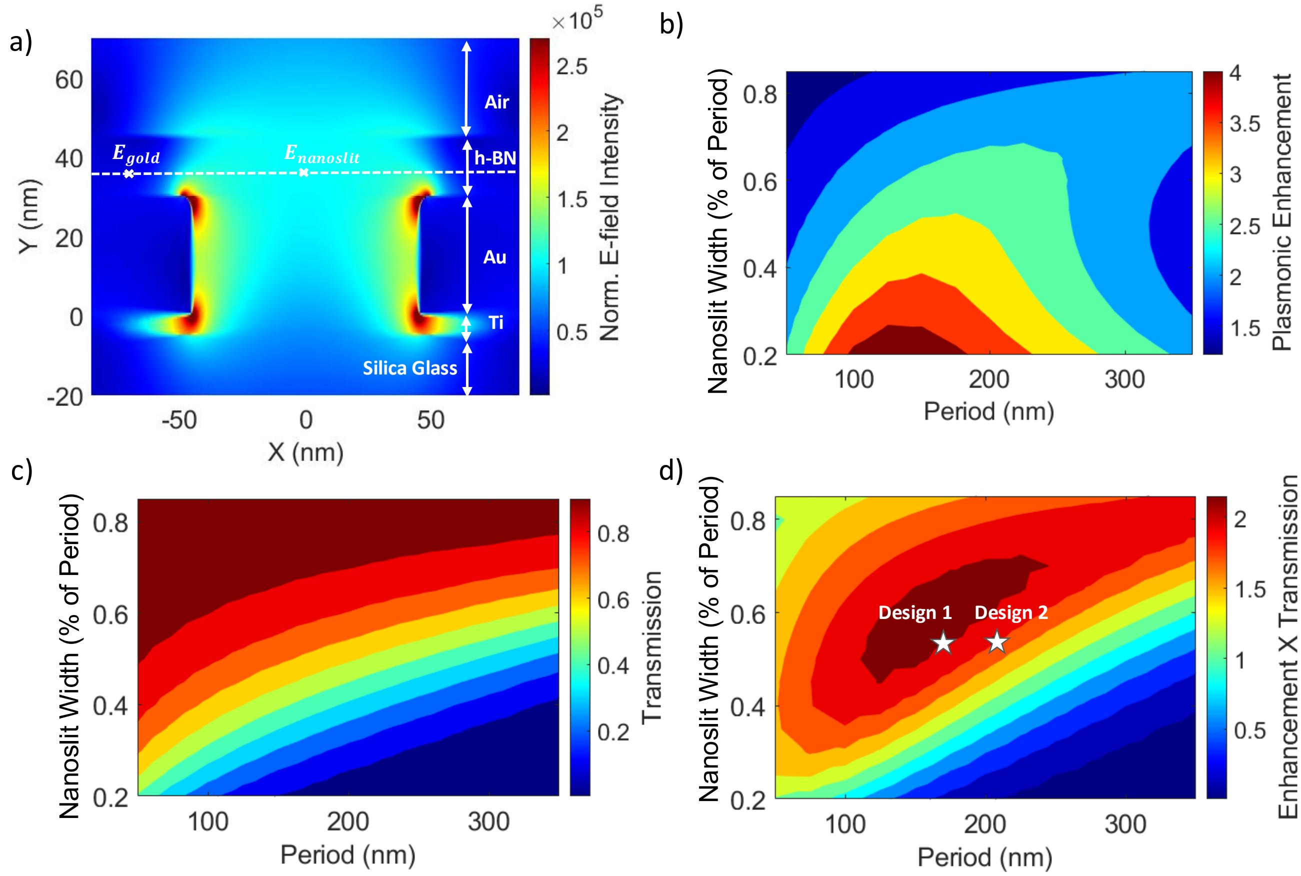

Supplementary Figure 1: **COMSOL simulations to optimize optical performance of the nanoslit array design for hBN thickness = 15 nm and V_B^- implantation depth = 10 nm.** (a) The simulation set-up for the nanoslit array design. An x-polarized plane wave is used for excitation through the silica glass. Enhanced normalized E-field intensity is observed at the gold nanoslit-air-hBN interface. The plasmonic enhancement is calculated by taking a ratio of $E_{nanoslit}/E_{gold}$. Implantation depth of V_B^- defects is marked using the white dotted line. (b) The effect of nanoslit width and period on the plasmonic enhancement. (c) The effect of nanoslit width and period on transmission through the nanoslit. (d) Contour plot showing the most optimized design for backward PL collection. The product of plasmonic enhancement and transmission is plotted against varying period length and nanoslit width. Both Design 1 (c = 170 nm, a = 90 nm) and Design 2 (c = 210 nm and a = 110 nm) are optimized.

For 15 nm thick hBN flakes, we observed a substantially greater plasmonic enhancement from the nanoslit array (Supplementary Figure 1(a)) compared to the 30 nm-thick hBN flakes shown in Supplementray Figure 2(a). Supplementary Figure 1(b) illustrates how the period and nanoslit width influence plasmonic enhancement, with the highest enhancement occurring at low period lengths and narrow nanoslit widths. This behavior aligns with expectations, as enhancement is strongest at the corners of the gold nanoslit and hBN interface. Conversely, transmission through the nanoslit is maximized when the nanoslit width constitutes a larger percentage of the period, as depicted in Supplementary Figure 1(c). Supplementary Figure 1(d) presents the combined effect of period and nanoslit width on the product of plasmonic enhancement and nanoslit transmission. Here, Design 1 corresponds to a period of $c = 170$ nm and a nanoslit width of $a = 90$ nm (52.9% of the period), while Design 2 represents the configuration used for imaging nickel nanoparticles, with $c = 210$ nm and $a = 110$ nm (52.4% of the period).

We can see that both designs are well optimized for maximum photoluminescence collection from the backside of the device.

To further investigate the impact of hBN flake thickness on optical performance, we conducted the same set of simulations using 30 nm-thick hBN, setting the average defect implantation depth to 25 nm (Supplementary Figure 2). The results show a significant reduction in plasmonic enhancement due to the increased thickness. While the overall trends in plasmonic enhancement and transmission as functions of period length and nanoslit width remain consistent with the previous case (Supplementary Figures 2 (b) and (c)), the product of enhancement and transmission becomes increasingly governed by the transmission behavior alone. Optimizing the device under these conditions would require fabricating a nanoslit array with narrower periods and wider nanoslit widths. However, such geometries are not only difficult to achieve from a fabrication perspective, but they would also lead to higher device resistance, increasing the risk of thermal damage such as burning or melting. Therefore, we opted to use the original design, which is well-suited for flakes thinner than 15 nm.

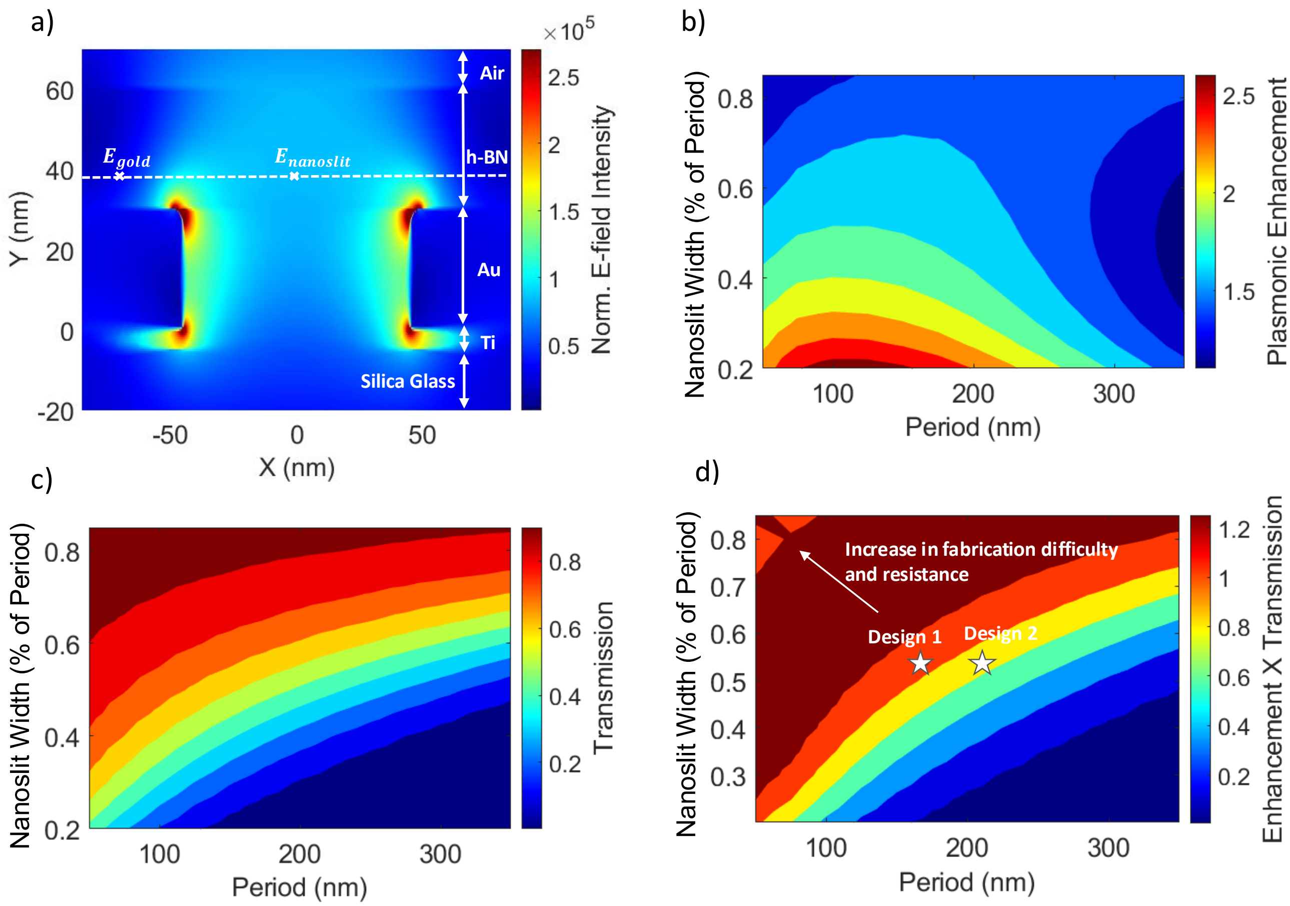

Supplementary Figure 2: **COMSOL simulations to optimize optical performance of the nanoslit array design for hBN thickness = 30 nm and V_B^- implantation depth = 25 nm.** (a) Normalized E-field intensity is enhanced at the gold-hBN-air interface, but dies off quickly due to the thicker hBN flake. Implantation depth of V_B^- defects is marked using the white dotted line. (b) The effect of nanoslit width and period on the plasmonic enhancement. The magnitude of plasmonic enhancement for the same period and nanoslit width decreased significantly as compared to 15 nm-thick hBN. (c) The effect of nanoslit width and period on transmission through the nanoslit.(d) Contour plot showing the most optimized design for backward PL collection. The product of plasmonic enhancement and transmission is plotted against varying period length and nanoslit width. This behavior is now dominated by the transmission, due to the drastic reduction in plasmonic enhancement. However, the more optimized designs have higher device resistance and increased difficulty in fabrication process.

Microwave Simulations

We performed COMSOL simulations to evaluate the microwave performance of the fabricated coplanar waveguide and to investigate how the etched nanoslit array influences microwave delivery efficiency. All simulations are done for 2.7 GHz microwave frequency.

The simulated structure consisted of a microwave coplanar waveguide patterned on a 100 μm-thick sapphire substrate, with a 2 mm signal trace width and a 0.18 mm gap width.

As shown in Supplementary Figure 3(a), we modeled a 30 nm-thick gold film incorporating the nanoslit array (Design 1 in the main text), with slit dimensions of $a = 90$ nm, $b = 1$ μm, and $c = 170$ nm. The magnetic field distribution was evaluated in a horizontal slice located 20 nm above the gold surface, corresponding to the typical thickness of exfoliated hBN flakes and the depth of the V_B^- defects.

The simulations indicate that the x-component of the magnetic field (B_x), which drives Rabi oscillations, is spatially inhomogeneous across the nanoslit array. This inhomogeneity can contribute to faster damping of the Rabi oscillations. We further observe that increasing the nanoslit length (b = 2.5 μm) does not affect the non-uniformity of the B_x field (Supplementary Figure 3(b)).

To mitigate this inhomogeneity, we examined the effect of increasing the gold film thickness. As shown in Supplementary Figure 3(c), a thicker gold layer of 50 nm gold partially improves the uniformity of microwave delivery across the nanoslit array.

In Supplementary Figure 4(a) and (b), we compare cross-sectional profiles of Design 1 with 30 nm and 50 nm gold layers. The results show that increasing the gold thickness to 50 nm reduces the spatial inhomogeneity of the B_x field compared to the 30 nm case.

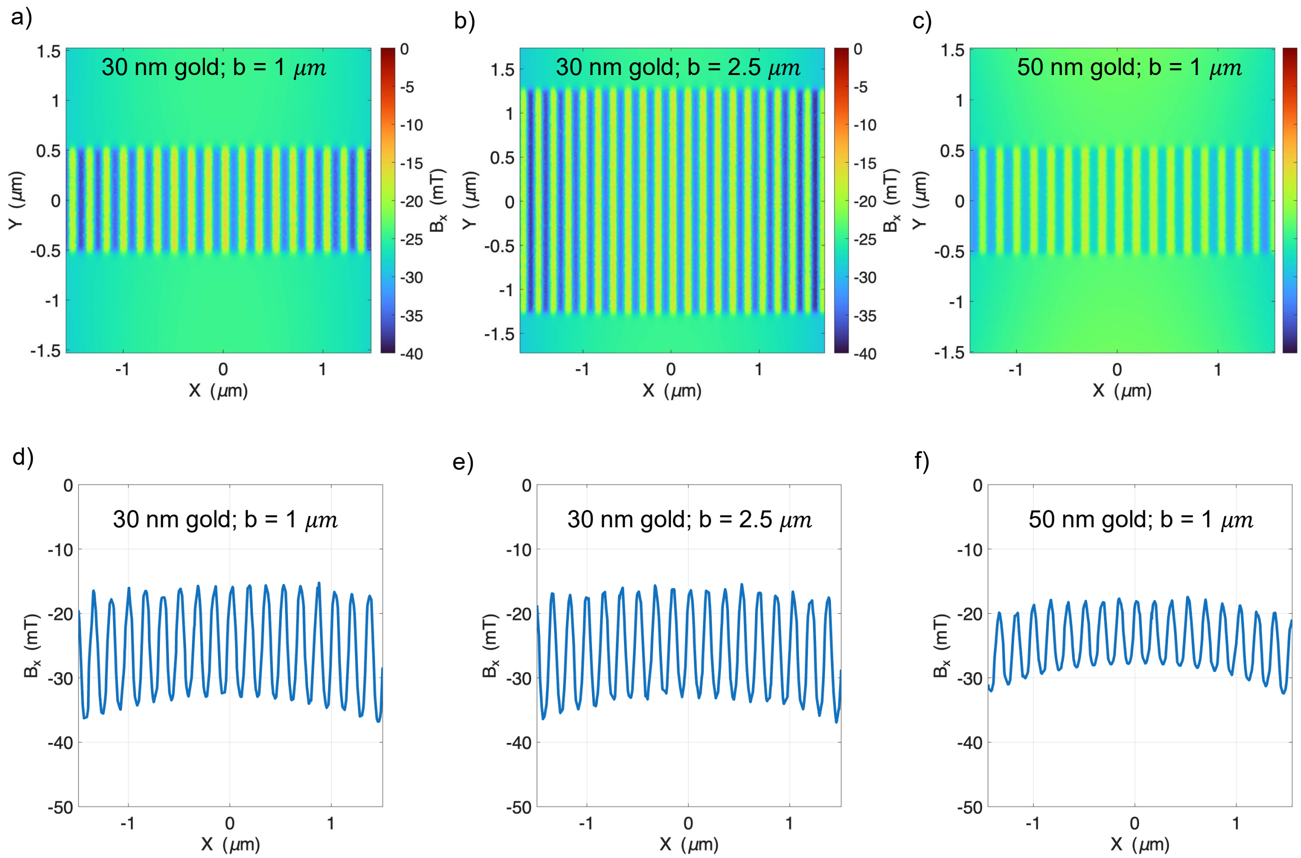

Supplementary Figure 3: **COMSOL simulations for the microwave performance of the nanoslit array for different array lengths and gold layer thicknesses.** (a) Simulation of the distribution of the B_x field over the nanoslit array for Design 1. The field is inhomogeneous over the patterned array. (b) The same simulation is performed, with b being increased from 1 μm to 2.5 μm. The inhomogeneity does not change with change in b. (c) Increasing the thickness of gold for Design 1 reduces the spatial inhomogeneity of the B_x field, as is shown by the simulation done for 50 nm gold layer. (d),(e),(f) We quantify the variation by plotting the B_x field vs X while setting Y=0. It is evident that the spatial inhomogeneity for the B_x field is least for Design 1 with 50 nm gold thickness.

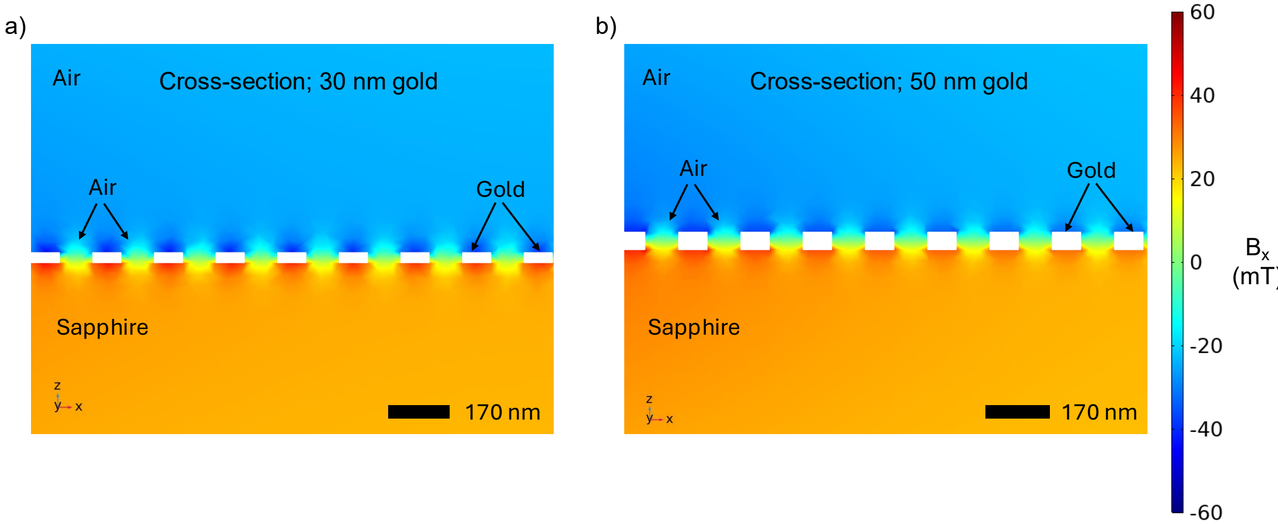

Supplementary Figure 4: **Cross-sectional Profile of B_x field for Design 1 with gold layer thicknesses of 30 nm and 50 nm** Distribution of B_x field in the x-z plane for Design 1 with (a) 30 nm thick gold layer and (b) 50 nm thick gold layer. The white spaces represent gold metal layer. Spatial inhomogeneity in the z direction is lower for the 50 nm case as compared to the 30 nm case.

Rabi Oscillation Data

We also present Rabi oscillation measurements for two devices with identical geometrical parameters (Design 1) but different gold thicknesses: 30 nm and 50 nm. We note that the 30 nm device contains dispersed nickel nanoparticles, which may contribute additional magnetic noise and accelerate Rabi decay.

As shown in Supplementary Figure 5(a) and (b), the Rabi oscillations measured on the nanoslit pattern for the 50 nm gold device exhibit a lower Rabi frequency and faster dephasing compared to the off-pattern regions.

For the 30 nm gold device (Supplementary Figure 5(c) and (d)), the oscillations on the nanoslit array decay more rapidly. This behavior can be attributed to spatial inhomogeneity of the B_x field, as well as magnetic spin noise from nearby nickel nanoparticles. Despite the enhanced damping, the first oscillation remains clearly resolved, allowing us to determine the π-pulse duration used for the T_1 relaxometry measurements presented in the main text.

Importantly, the Rabi contrast is comparable between on-pattern and off-pattern regions for both 30 nm and 50 nm devices, enabling efficient CW-ODMR measurements on the nanoslit array.

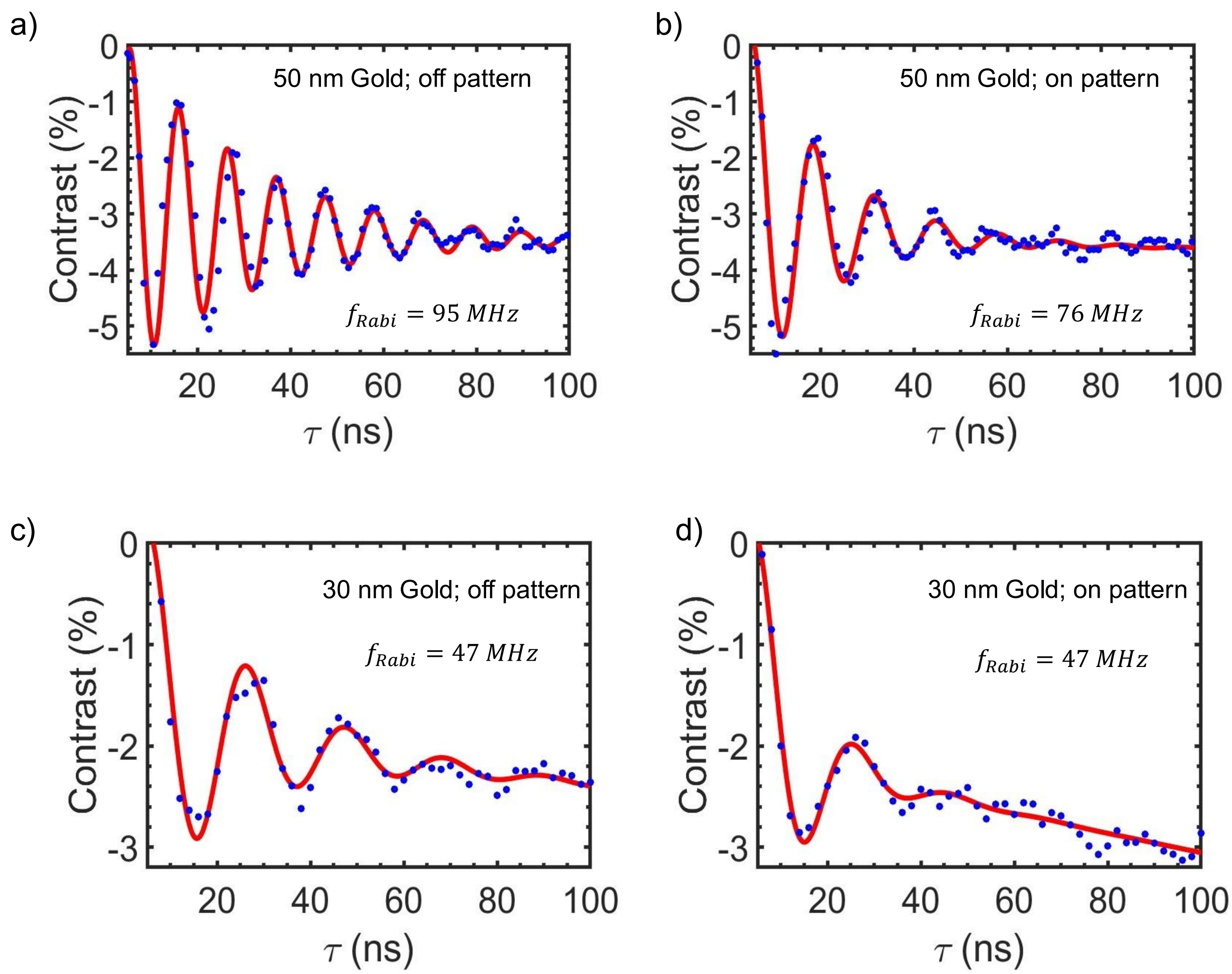

Supplementary Figure 5: **Rabi oscillation data for two devices : 30 nm and 50 nm gold layers.** Panels (a) and (b) compare the Rabi oscillations measured off and on the nanoslit pattern, respectively, for the 50 nm device. The oscillations on the nanoslit pattern exhibit a reduced Rabi frequency and faster decay. Panels (c) and (d) present the corresponding measurements for the 30 nm device, showing a similar trend.